Dark Excitons



# Dark-Exciton-Mediated Fano Resonance from a Single Gold Nanostructure on Monolayer WS<sub>2</sub> at Room Temperature

Mingsong Wang, Zilong Wu, Alex Krasnok, Tianyi Zhang, Mingzu Liu, He Liu, Leonardo Scarabelli, Jie Fang, Luis M. Liz-Marzán, Mauricio Terrones, Andrea Alù, and Yuebing Zheng\*

Strong spatial confinement and highly reduced dielectric screening provide monolayer transition metal dichalcogenides with strong many-body effects, thereby possessing optically forbidden excitonic states (i.e., dark excitons) at room temperature. Herein, the interaction of surface plasmons with dark excitons in hybrid systems consisting of stacked gold nanotriangles and monolayer  $WS_2$  is explored. A narrow Fano resonance is observed when the hybrid system is surrounded by water, and the narrowing of the spectral Fano linewidth is attributed to the plasmon-enhanced decay of dark K-K excitons. These results reveal that dark excitons in monolayer  $WS_2$  can strongly modify Fano resonances in hybrid plasmon—exciton systems and can be harnessed for novel optical sensors and active nanophotonic devices.

1. Introduction

Owing to its significant field enhancement and narrow linewidth, Fano resonances in plasmonic nanostructures have great potential for applications in sensing, nonlinear optics, and nanolasers.<sup>[1–5]</sup> Many theoretical and experimental works have been

carried out to explore Fano resonances that arise from the coupling between surface plasmons (SPs) and excitons in quantum dots (QDs) or dye molecules.[2,6-11] However, the lack of efficient ways to actively tune the excitonic properties of QDs and dye molecules near plasmonic nanostructures makes the development of active devices based on hybrid plasmon-QD/ dye systems challenging. Recently, the interaction between plasmonic nanostructures and emerging 2D semiconductors, including monolayer transition metal dichalcogenides (TMDCs), has attracted the attention of various researchers.[12-14] monolayer TMDCs possess high carrier

mobility, direct bandgap, and strong excitonic and mechanical properties. Combining these outstanding properties with plasmonic nanostructures, able to confine light at the subwavelength scale and generate energetic hot electrons, holds the promise to enhance the performance of monolayer TMDC-based optoelectronic components and boost the development of miniaturized

Dr. M. Wang, Dr. Z. Wu, J. Fang, Prof. Y. Zheng Department of Mechanical Engineering Texas Materials Institute The University of Texas at Austin Austin, TX 78712, USA E-mail: zheng@austin.utexas.edu Dr. A. Krasnok, Prof. A. Alù Photonics Initiative Advanced Science Research Center Physics Program Graduate Center Department of Electrical Engineering City College of the City University of New York New York, NY 10031, USA T. Zhang, M. Liu, H. Liu, Prof. M. Terrones Department of Materials Science and Engineering Department of Physics Department of Chemistry Center for 2-Dimensional and Layered Materials The Pennsylvania State University University Park

Department of Chemistry and Biochemistry California NanoSystems Institute University of California, Los Angeles Los Angeles, CA 90095, USA Prof. L. M. Liz-Marzán Bionanoplasmonics Laboratory CIC biomaGUNE Paseo de Miramón 182, 20014 Donostia-San Sebastián, Spain Prof. L. M. Liz-Marzán Ikerbasque Basque Foundation for Science 48013 Bilbao, Spain Prof. L. M. Liz-Marzán Biomedical Research Networking Center in Bioengineering Biomaterials, and Nanomedicine CIBER-BBN 20014 Donostia-San Sebastián, Spain

The ORCID identification number(s) for the author(s) of this article can be found under https://doi.org/10.1002/smll.201900982.

DOI: 10.1002/smll.201900982

Dr. L. Scarabelli

PA 16802, USA

and flexible optical devices. For example, plasmonic nanostructures can induce large photoluminescence enhancement of monolayer TMDCs via strongly enhanced local electric fields (E-fields) and Purcell phenomena.[15,16] Electrons and energy can be transferred from plasmonic nanostructures to monolayer TMDCs through hot-electron injection and resonance energy transfer, respectively.[17-19] Coupling between exciton states of monolayer TMDCs and localized plasmon resonances (LSPRs) can lead to Fano resonance and even strong plasmon-exciton coupling.[20-26] Furthermore, because of the large exciton binding energy and weak dielectric screening, monolayer TMDCs have an outstanding tunability regarding their excitonic properties. This tunability further endows hybrid plasmon–TMDC systems with an ability to control Fano interference between surface plasmons and excitons. For example, the tuning of Fano resonance in hybrid plasmon-WS2 systems has been demonstrated through varying the static dielectric constant of the surrounding media.<sup>[20]</sup>

The strong spatial confinement and low dielectric screening of monolayer TMDCs also endow them with exotic excitonic properties, when compared to conventional QDs and dye molecules. For example, density functional theory (DFT) calculations involving many-body perturbation and the Betha-Salpeter equation have unraveled significant many-body effects in monolayer TMDCs.<sup>[27]</sup> The many-body effects together with the strong spin-orbit coupling in monolayer TMDCs lead to the formation of optically forbidden excitonic states (i.e., dark excitons).[28-30] Dark excitons in monolayer TMDCs are interesting due to their long lifetimes and strong coupling with bright excitons, thus having great potential in Bose-Einstein condensation, optoelectronic devices, and sensing.[28,31-33] For this reason, monolayer TMDCs constitute a promising platform to explore how dark excitons influence plasmonexciton coupling. However, current studies of excited states in monolayer TMDCs mainly focus on bright excitons. How the coupling between dark excitons and LSPRs influences the optical properties of monolayer TMDCs remains essentially unexplored. In this paper, we demonstrate that the coupling between dark excitons in monolayer WS<sub>2</sub> and out-of-plane LSPRs can strongly affect the spectral linewidth of Fano resonances in hybrid plasmon–exciton systems.

## 2. Results and Discussion

Chemically synthesized gold nanotriangles with an edge length of ≈55 nm (55 nm AuNTs) were selected because: (1) they feature atomically flat surfaces, which ensure a strong interaction between AuNTs and monolayer TMDCs; (2) the interaction between them and monolayer WS2 can lead to an asymmetric Fano spectral profile, compared to larger AuNTs, such as 150 nm AuNTs. AuNTs were synthesized following a previously reported seed-growth method,[34] and the detailed discussion about how the size of AuNTs affects the Fano resonance was reported in our previous study.[20] It should be noticed that there is a layer of cetyltrimethylammonium chloride (CTAC) molecules covering the AuNTs, which prevents direct electron transfer between AuNTs and monolayer TMDCs. Monolayer 1H-WS<sub>2</sub> flakes were grown on SiO<sub>2</sub>/Si substrates via chemical vapor deposition (CVD) and were then transferred onto glass slides (detailed information of monolayer WS2 synthesis is provided in the Experimental Section).

Representative optical and atomic force microscope (AFM) images of monolayer WS<sub>2</sub> are shown in Figure S1 (Supporting Information). From the recorded height profiles, we determined a thickness of 0.9 nm, corresponding to a monolayer WS<sub>2</sub> flake on a glass substrate. [35–38] An inverted optical microscope equipped with a spectrometer, as schematically illustrated in **Figure 1**a, was employed to acquire single-nanoparticle

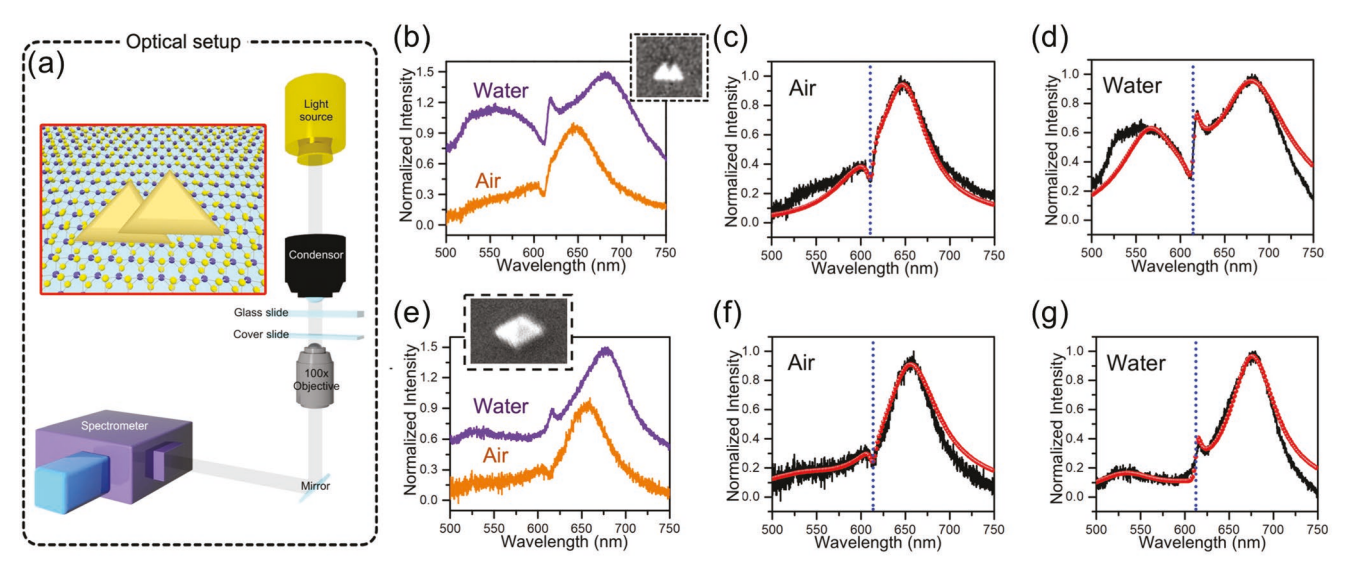


Figure 1. a) Schematic diagram of the optical setup. Inset is the schematic illustration of SA 1 on monolayer  $WS_2$ . b) Scattering spectra of SA 1 on monolayer  $WS_2$  in the air (orange curve) and water (purple curve). Shown in the inset is a SEM image of SA 1. c,d) Fano fitting of scattering spectra of SA 1 on monolayer  $WS_2$  in the air and water. e) Scattering spectra of SA 2 on monolayer  $WS_2$  in the air (orange curve) and water (purple curve). Shown in the inset is a SEM image of SA 2. f,g) Fano fitting of scattering spectra of SA 2 on monolayer  $WS_2$  in the air and water. The blue dotted lines in (c), (d), (f), and (g) indicate the peak positions of A excitons.

www.small-journal.com

**Table 1.** Values of q,  $\delta$  and linewidth obtained from Fano fitting and linewidth obtained from CMT fitting.

Surrounding medium	9	δ	Linewidth (Fano)	Linewidth (CMT)
SA 1				
Air	-0.25	$0.58\pi$	31.4 meV	28.1 meV
Water	-0.93	$0.74\pi$	20.8 meV	22.3 meV
SA 2				
Air	0.00	$0.50\pi$	29.8 meV	33.1 meV
Water	-0.70	$0.69\pi$	24.8 meV	33.9 meV

scattering spectra (details of optical measurements are provided in the Experimental Section). AuNTs were drop-casted on the surface of monolayer WS<sub>2</sub>.

The inset in Figure 1a schematically shows the hybrid system of stacked AuNTs on monolayer WS2. The stacked configuration is formed during the drop-casting process with one edge of a 55 nm AuNT partially overlapping the one of the other AuNT (scanning electron microscopy (SEM) images of two stacked AuNTs (SA 1 and SA 2) on monolayer WS2 are shown as insets in Figure 1b,e). Figure 1b,e indicates that scattering spectra of SA 1 (SA 2) in air and water have a peak at ≈650 nm (≈656 nm) and ≈681 nm (≈677 nm). The scattering spectra were obtained by a dark-field microscope setup with an EMCCD (detailed information is the Experimental Section). To analyze the origin of these peaks, we simulated the scattering spectra of stacked AuNTs on a glass substrate through a finitedifference time domain (FDTD) method. The FDTD simulation results in the Supporting Information indicate that the scattering peaks are associated with the excitation of plasmonic dipole modes.

Scattering spectra in Figure 1b,e also illustrate a clear evolution from a symmetric scattering dip to an asymmetric Fano lineshape at the resonance peak of the A exciton (≈615 nm), when the surrounding medium is changed from air to water. Adding water itself does not change a symmetric spectral profile into an asymmetric one. But it varies the interaction between A excitons and LSPRs, which can lead to the asymmetric Fano resonance, by increasing the total dipole moment of A excitons of monolayer WS2. [20] Thus, the asymmetric Fano profile is brought by changing the interaction between A excitons and LSPRs. When compared to an individual AuNT on monolayer WS2, the stacked AuNTs possess a narrower asymmetric Fano resonance.<sup>[20]</sup> The maximum value of the asymmetric Fano resonance is at  $E_{\text{max}} = E_{\text{F}} + \Gamma/(2q)$ , the minimum is located at  $E_{\min} = E_F - \Gamma q/2$ , and the width of the resonance is proportional to  $E_{\text{max}} - E_{\text{min}}$ , where  $E_{\text{F}}$  is the resonant energy,  $\Gamma$  is the width of the discrete state, and q is the Fano asymmetry parameter. This suggests that the narrower Fano lineshape reveals a smaller resonance linewidth of A excitons coupled to the stacked AuNTs than the one of regular A excitons.[2]

To interpret the observed spectral change, we fitted the scattering spectra with a Fano approach developed by Gallinet and  $Martin^{[20,39]}$ 

$$\sigma_{\text{scat}}(\omega) = \sigma_{\text{ex}}(\omega)\sigma_{\text{pl}}(\omega) \tag{1}$$

where  $\omega$  is the frequency and  $\sigma_{scat}(\omega)$  is the scattering cross section.  $\sigma_{ex}(\omega)$  is the excitonic (dark) mode and  $\sigma_{pl}(\omega)$  is the plasmonic (bright) mode that is defined as a function of  $\omega$  with a symmetric pseudo-Lorentzian line shape. They are given by

$$\sigma_{\text{ex}}(\omega) = \frac{\left(\frac{\omega^2 - \omega_{\text{ex}}^2}{\Gamma_{\text{ex}}\omega_{\text{ex}}} + q\right)^2 + b}{\left(\frac{\omega^2 - \omega_{\text{ex}}^2}{\Gamma_{\text{ex}}\omega_{\text{ex}}}\right)^2 + 1}, \quad \sigma_{\text{pl}}(\omega) = \frac{a^2}{\left(\frac{\omega^2 - \omega_{\text{pl}}^2}{\Gamma_{\text{pl}}\omega_{\text{pl}}}\right)^2 + 1}$$
(2)

where  $\omega_{\rm ex}$ ,  $\Gamma_{\rm ex}$  and  $\omega_{\rm pl}$ ,  $\Gamma_{\rm pl}$  are the resonant frequency and the width of resonance line at half maximum of the exciton and plasmonic resonances, respectively, b is the damping parameter originating from intrinsic losses, a is the maximal amplitude of the resonance. The fitting curves are shown in Figure 1c-f, and the fitting parameters are listed in Table 1. The results reveal that for the SA 1 (SA 2) |q| increases from 0.25 to 0.93 (from 0.00 to 0.70) when the sample was covered by water. It is known that  $q = \cot(\delta)$ , where  $\delta$  is the phase of the time-dependent response function of the excitons, thus playing the role of the continuum at the SP resonance.<sup>[40]</sup> The corresponding phases obtained from the above Fano fitting for the sample in air and water are  $0.58\pi$  and  $0.74\pi$  ( $0.50\pi$  and  $0.69\pi$ ), respectively. This result is consistent with an increase in the q of a single AuNT on monolayer WS<sub>2</sub> when the static dielectric constant increases, as reported in our previous study.[20]

The resonance linewidth values of A excitons listed in Table 1 (31.4 and 29.8 meV in the air and 20.8 and 24.8 meV in water) are smaller than the reported value of bare monolayer WS<sub>2</sub> ( $\approx$ 60 meV). [20,41,42] It should be noted that the results of the Fano fitting are based on dark-field scattering measurements and thus do not represent the total scattering of plasmonic nanostructures. But this does not affect the values of the resonance linewidth of A excitons, because they are determined by  $\sigma_{\rm ex}(\omega)$ , which is not influenced by the radiation pattern of plasmonic nanostructures. To further analyze the experimental result and confirm the reduced resonance linewidth, we applied a modified coupled harmonic oscillator model theory (CMT) to fit our experimental results. CMT has been used to describe the plasmonic analogue of electromagnetically induced transparency (EIT), as well as strong coupling in plasmonic nanostructures.<sup>[43]</sup> However, in the conventional CMT approach, it is assumed that SPs drive the excitons and the coupled oscillators have the same phase. Thus, the conventional CMT approach cannot be directly used to analyze asymmetric Fano profiles. A phase difference between excitons and SPs should be considered (detailed discussion in the Supporting Information), and the corresponding scattering cross section obtained from the modified CMT is

$$\sigma_{\text{scat}} \propto \left| \frac{\omega^2 \tilde{\omega}_{\text{ex}}^2}{\tilde{\omega}_{\text{ol}}^2 - \omega^2 \tilde{g}^2 e^{-2i\varphi}} \right|^2 \tag{3}$$

where e is the elementary charge,  $\tilde{g}$  is the plasmon–exciton coupling strength, and  $\varphi$  is the phase difference between SPs and the total moment of excitons,  $\tilde{\omega}_{\rm ex}^2 = (\omega^2 - \omega_{\rm ex}^2 + i\Gamma_{\rm ex}\omega)$ ,  $\tilde{\omega}_{\rm pl}^2 = (\omega^2 - \omega_{\rm pl}^2 + i\Gamma_{\rm pl}\omega)$ . The results obtained by this fitting are

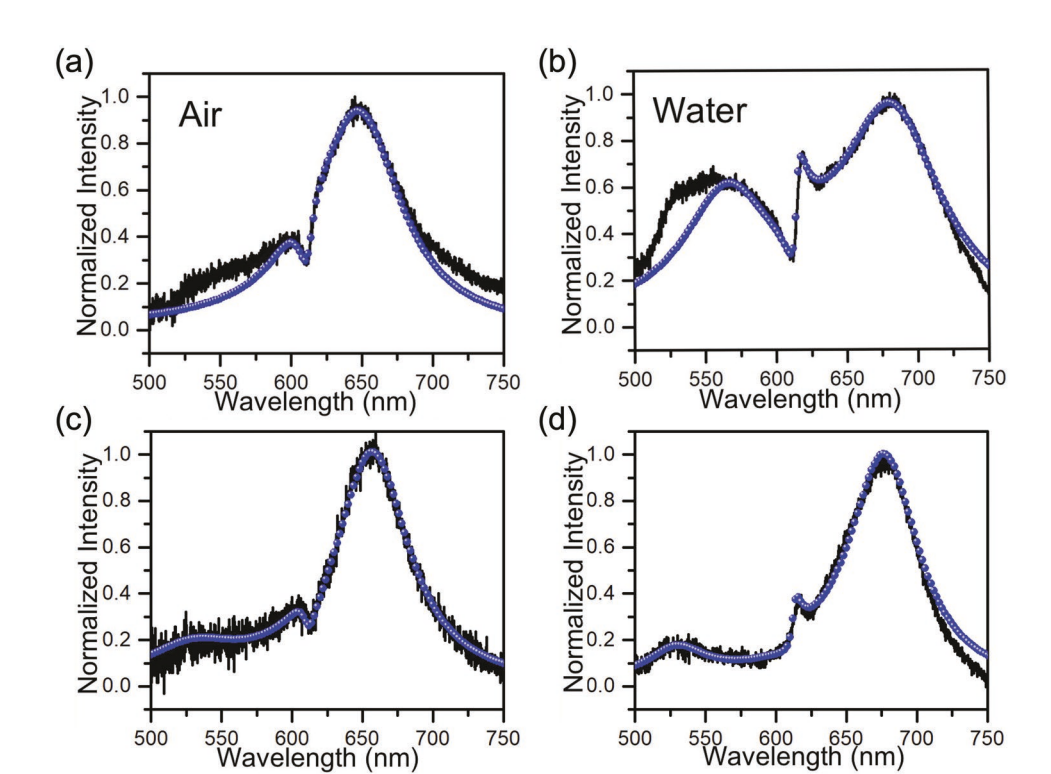


Figure 2. CMT fitting of scattering spectra of SA 1 (SA 2) on monolayer WS<sub>2</sub> in the air (a (c)) and water (b (d)).

plotted in Figure 2a-d, matching the experimental results. The calculated values of the resonance linewidth of A excitons are 28.1 and 33.1 meV in air and 22.3 and 33.9 meV in water, which are in good agreement with those obtained from the Fano fitting. It should be stressed that q and b have different physical meanings than  $\tilde{g}$  and  $\varphi$ . This difference limits these free fitting parameters and it is one of the reasons why we chose two different methods to fit the experimental results in order to get a more accurate conclusion. It is also found that  $\,\tilde{g}\,$  for the SA 1 (SA 2) is increased from 74.4 meV (53.8 meV) to 95.1 meV (68.2 meV) when the surrounding medium changes from air to water. However,  $2\tilde{g}$  for both air and water are smaller than the total loss of the whole system (234.9 meV (223.3 meV) for air and 253.9 meV (191.1 meV) for water), which means that the coupling between the SA 1 (SA 2) and monolayer WS2 does not reach the strong coupling regime when covered by either air or water.

Recently, Selig et al. have theoretically and experimentally reported that the resonance linewidth of A excitons can be controlled by decay channels from A excitons to intervalley dark excitons. [32] Dark excitons of monolayer WS<sub>2</sub> include intravalley dark *K-K* excitons (spin-forbidden excitons) and intervalley dark *K-K'* and *K-*Λ excitons (momentum-forbidden excitons), as shown in **Figure 3a**. [28,32,33,44–46] It should be noticed that because at room temperature the photon scattering is faster than the spin flip process, the spin-forbidden transfer from A excitons to dark *K-K* states is negligible in this study. [28,32] The resonance linewidth of A excitons in monolayer WS<sub>2</sub> is mainly affected by the radiative and nonradiative decay rate of A excitons ( $\gamma_{rad}$  and  $\gamma_{nonrad}$ ) and A excitons to *K-*Λ states rate ( $\gamma_{K-\Lambda}$ ) (all the decay channels are schematically illustrated in Figure 3b),

while the A excitons to K-K' states rate ( $\gamma_{K-K'}$ ) has a minor contribution to the spectral linewidth owing to the weak electron—phonon coupling element.<sup>[32]</sup>

In addition, dark K-K' excitons degenerate energetically with dark K-K excitons.[33] Therefore, when the decay rate of dark K-K excitons  $X_D-\gamma_{X_D}$  increases, the degeneration of dark K-K' excitons is enhanced. Park et al. have demonstrated that out-ofplane LSPRs profoundly enhance the spontaneous decay rate of dark K-K excitons with a large Purcell factor of  $\geq 2 \times 10^3$ , while leaving the decay rates of in-plane A excitons and dark  $K-\Lambda$  excitons unenhanced. [47] This result implies that the spectral linewidth of A excitons can be controlled by inducing the coupling between out-of-plane LSPRs and dark K-K excitons. The plasmon-enhanced decay of dark K-K excitons boosts the A excitons to K-K' states transfer and leads less A excitons decay through the K-K and K- $\Lambda$  decay channels, resulting in the resonance linewidth of A excitons ascribed to the K-K and  $K-\Lambda$ decay channels to reduce, as schematically shown in Figure 3c. Figure 3d further illustrates that the reduced resonance linewidth of A excitons can bring a narrower Fano profile in the scattering spectrum of the hybrid system of a single plasmonic nanoparticle on WS2 in water. Thus, we conclude that the decrease in spectral linewidth may be brought by the coupling between LSPRs on the stacked AuNTs and dark K-K excitons. In order to verify this assumption, we simulated the scattering spectra and electromagnetic field distribution of the stacked AuNTs using the finite-difference time-domain (FDTD) method (detailed information is in the Supporting Information). Herein, we use SA 1 as an example and the detailed analysis of SA 2 is in the Supporting Information. It should be noticed that the edges of AuNTs are not flat, as shown in Figure 4a,b. The

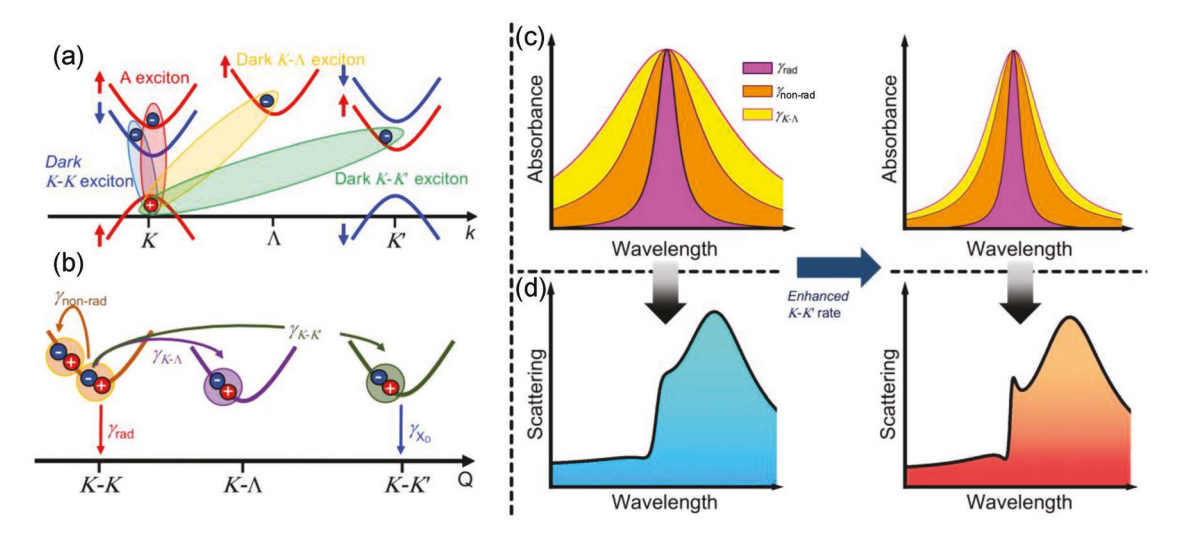


Figure 3. a) Schematic electronic dispersions at the K, K', and  $\Lambda$  point. The bright A exciton, intravalley dark K-K exciton, intervalley dark K-K', and K- $\Lambda$  exciton are enclosed by a red, blue, green, and yellow oval, respectively. k is the wave vector and red and blue arrows show the direction of the electronic spin. b) Schematic diagram of the minima of the excitonic center-of-mass motion (Q) dispersion E(Q). The arrows illustrate the decay channels of A excitons: the radiative decay ( $\gamma_{rad}$ ) (red), nonradiative decay ( $\gamma_{ronrad}$ ) (brown), the A excitons to K- $\Lambda$  states ( $\gamma_{K-\Lambda}$ ) (purple) transfer, and the A excitons to K-K' states ( $\gamma_{K-K'}$ ) transfer (green). The blue arrow represents the decay of the dark K-K excitons ( $\gamma_{X-\rho}$ ). c) Schematic diagram showing that the enhanced  $\gamma_{K-K'}$  leads to a reduced spectral linewidth of A excitons. d) Schematic diagram showing that the reduced spectral linewidth of A excitons leads to a narrower Fano profile in the scattering spectrum of the hybrid system in water.

E-field distributions and their x components in Figure 4d–g manifest that under parallel polarized light, SA 1 possesses out-of-plane dipoles at the resonance peak ( $\approx$ 630 nm) of dark K-K excitons (about 47 meV below A excitons) in both air and water. He figures S9 and S10 (Supporting Information) show SA 2 possesses out-of-plane dipoles at 630 nm under both parallel and vertically polarized light. Thus, the vertical dipole of SA 1 and 2 can effectively couple with the out-of-plane dark K-K excitons and enhance  $\gamma_{X_D}$ . The enhanced  $\gamma_{X_D}$  boosts  $\gamma_{K$ -K', which reduces the spectral linewidth.

The in-plane SPs of SA 1 and 2 can also enhance the radiative and nonradiative decay rates of A excitons, thus leading to an increase in spectral linewidth. Therefore, in order to determine whether the coupling between stacked AuNTs and monolayer WS<sub>2</sub> leads to a reduced or increased resonance linewidth of A excitons, we compare the plasmon-induced enhancements in the dark *K-K* exciton decay rate ( $\gamma_{x_0}$ ) with the one of the A exciton decay rate ( $\gamma_{x_0}$ ). The Fermi's golden rule ensures that the spontaneous decay rate of emitters and total Purcell factors (radiative+nonradiative) are directly proportional

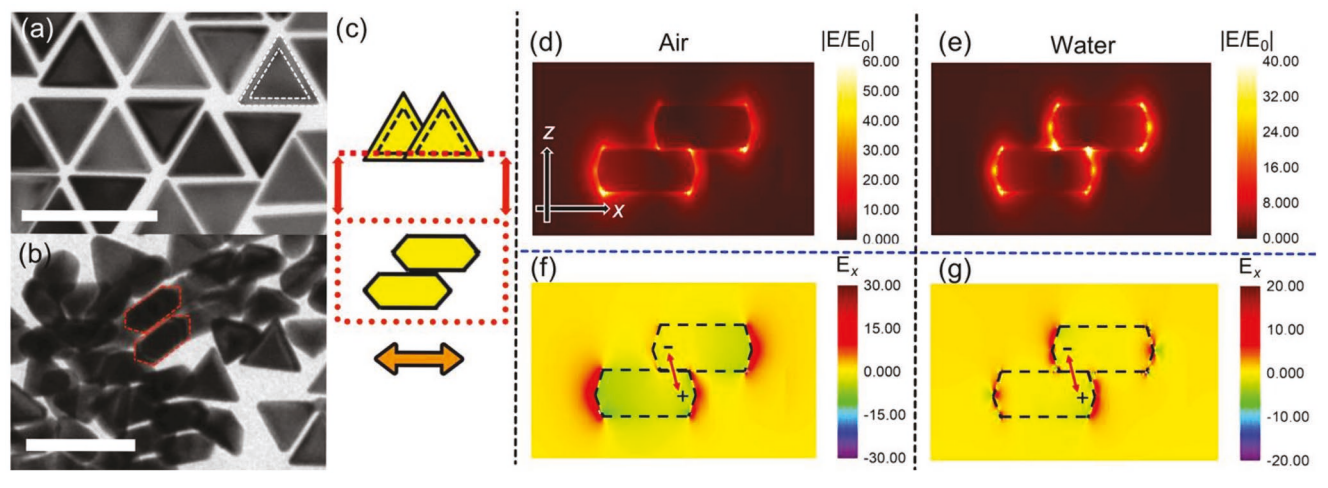


Figure 4. TEM images of AuNTs: a) The top view of AuNTs shows that there is a noticeable thickness change at the edge of AuNTs, which occurs at the region that is marked by the white dashed triangles; b) The red dashed polygons illustrate the contour profile of AuNTs, which unravel that the edge of AuNTs is not flat. Scale bars are 100 nm. c) Schematic images show where E-field is obtained (the red dotted line). The orange arrow shows the polarization of the incident light relative to SA 1. d,e) Simulated E-field distribution of SA 1 in the air and water, respectively. The wavelength of the incident light is 630 nm. f,g) Simulated distribution of x components of E-field in the air and water, respectively. The wavelength of the incident light is 630 nm. Positive and negative signs represent the distribution of positive and negative charges. The red arrow indicates the orientation of the dipole.

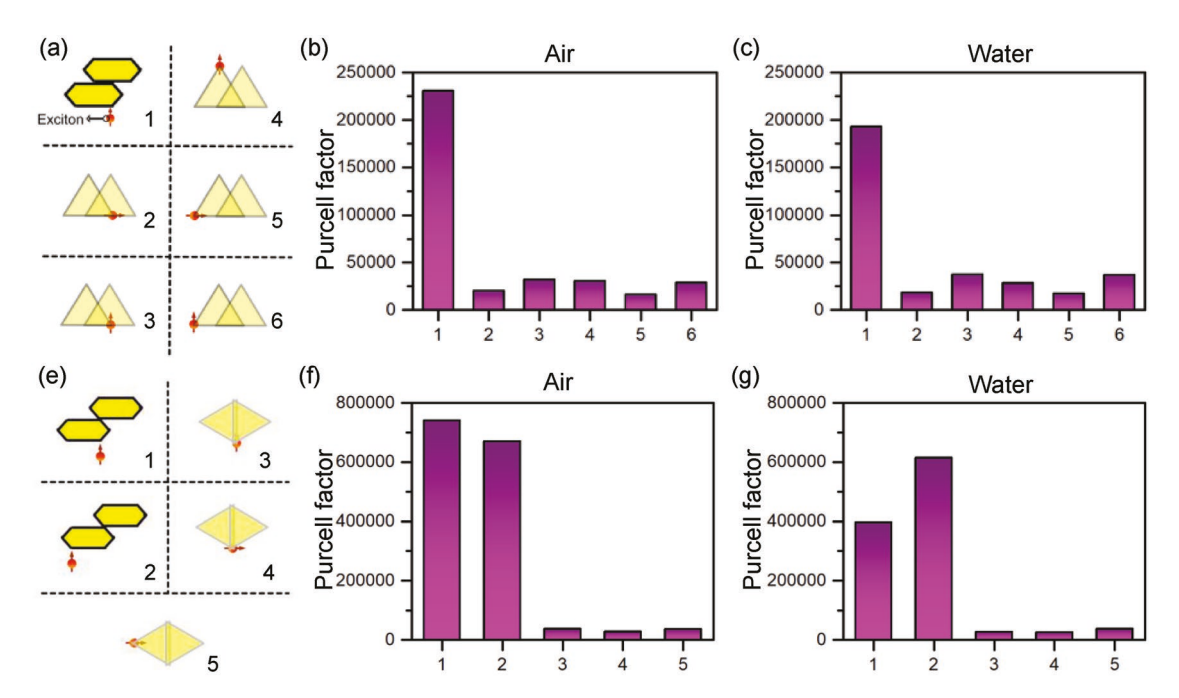


Figure 5. a) Schematic illustration of six different scenarios in the Purcell factor simulation for SA 1. b,c) Histogram of the simulated Purcell factors in the air and water. e) Schematic illustration of five different scenarios in the Purcell factor simulation for SA 2. f,g) Histogram of the simulated Purcell factors in the air and water. The dipole emitters are placed at 1 nm below the stacked AuNTs.

to the local density of states (LDOS). [48] Hence, the simulated Purcell factor can provide a comparison between the plasmoninduced enhancements in the decay rate. Six different scenarios for SA 1 and five different scenarios for SA 2 were considered, as schematically shown in Figure 5a,e. The choice of scenarios was based on the locations of the maximum field enhancement at 630 nm for the dark K-K exciton and 615 nm for the A exciton, as demonstrated by the corresponding E-field distributions in Figure 4 and Figures S4, S8-S10 (Supporting Information). For the SA 1 (SA 2), the first one (two) corresponds to the enhancement of  $\gamma_{X_D}$ , whereas others correspond to the enhancement in the sum of  $\gamma_{nonrad}$  and  $\gamma_{rad}$ . The obtained Purcell factors for SA 1 in the air (water) are  $2.31 \times 10^5$  ( $1.93 \times 10^5$ ),  $2.05 \times 10^4 \ (1.84 \times 10^4), \ 3.21 \times 10^4 \ (3.75 \times 10^4), \ 3.07 \times 10^4$  $(2.85 \times 10^4)$ ,  $1.64 \times 10^4$   $(1.74 \times 10^4)$ , and  $2.91 \times 10^4$   $(3.72 \times 10^4)$ , respectively (Figure 5b,c). While the obtained Purcell factors for SA 2 in the air (water) are  $7.41 \times 10^5$  (3.97 × 10<sup>5</sup>),  $6.71 \times 10^5$  $(6.14 \times 10^5)$ ,  $3.76 \times 10^4$   $(2.71 \times 10^4)$ ,  $2.80 \times 10^4$   $(2.63 \times 10^4)$ , and  $3.67 \times 10^4$  (3.79  $\times$  10<sup>4</sup>), respectively (Figure 5f,g). This indicates that, upon the excitation of LSPRs,  $\gamma_{X_D}$  reaches a larger enhancement than the sum of  $\gamma_{nonrad}$  and  $\gamma_{rad}.$  Therefore, the resonance linewidth of A excitons gets reduced, leading to a narrow asymmetric Fano resonance in the scattering spectrum.

#### 3. Conclusion

In summary, we observed a tunable transition from a symmetric dip at the resonance peak of the A exciton to a narrow asymmetric Fano lineshape in the scattering spectra of stacked AuNTs on monolayer WS<sub>2</sub>. The Fano fitting and CMT fitting unravel that in the hybrid system, where out-of-plane LSPRs couple with dark K-K excitons, A excitons show a reduced

spectral linewidth when compared to regular A excitons. The FDTD simulation and theoretical analysis reveal this result is derived from the plasmon-enhanced decay rate of dark K-K excitons via their coupling with the out-of-plane plasmonic mode in stacked AuNTs. Because A excitons to K-K' states transfer has a negligible contribution to the resonance linewidth of A excitons, the enhancement in  $\gamma_{X_D}$  reduces the resonance linewidth of A excitons. This makes the Fano interference between the stacked AuNTs and monolayer WS $_2$  to have a narrower spectral linewidth when compared to a single AuNT on monolayer WS $_2$ . Our result shows that the coupling between LSPRs and dark excitons can significantly modify the optical properties of monolayer TMDCs and paves the way for harnessing the plasmon-dark-exciton coupling for applications such as the biomedical sensing, optical modulators, and solar energy conversion.

## 4. Experimental Section

CVD Growth of Monolayer WS2: An atmospheric-pressure chemical vapor deposition (APCVD) approach was employed to synthesize monolayer WS2 on SiO2/Si substrate. [49] 5 mg of WO3 powders was first mixed with  $\approx\!0.5$  mg NaBr and then placed on a piece of the SiO2/Si wafer inside an alumina boat. Another SiO2/Si wafer was placed on the top of the boat facing down and then loaded inside a quartz tube. 400 mg sulfur in an alumina boat was placed on the upstream. The furnace was heated up to 825 °C and held for 15 min during synthesis. Meanwhile, a heating belt was used to heat sulfur powders to 250 °C separately. Argon with a flow rate of 100 sccm was used as the carrier gas. The AFM images and height profiles of CVD-grown monolayer WS2 were obtained through an AFM (Park Scientific). Monolayer WS2 was then transferred onto glass slides (VWR) via a poly(methyl methacrylate) (PMMA)-based transfer method. [20]

Synthesis of Gold Nanotringles: A standard CTAC/NaBH<sub>4</sub> procedure was used to prepare the initial Au seed solution.<sup>[34]</sup> Before use, the seed solution was kept for 2 h to consume excess borohydride. Following

SMQ

that, two different solutions were prepared for synthesizing the AuNTs. The first solution (solution 1) was prepared for growing Au seeds into larger nanoparticles, while the second solution (solution 2) was used as the AuNT growth batch. For example, to prepare 40 mL of 55 nm AuNT solution, 1.6 mL of a 0.1 M CTAC solution was added to 8 mL of Milli-Q water, followed by 40 μL of a 0.05 м HAuCl<sub>4</sub> solution and 15 μL of a 0.01 м Nal solution, to gain solution 1; 500 μL of a 0.05 м HAuCl<sub>4</sub> solution was added to 40 mL of 0.05 M CTAC, followed by 300  $\mu L$  of a 0.01 M NaI solution, to obtain solution 2. Before growing the AuNTs, a 0.1  $\,\mathrm{M}$  CTAC solution was used to dilute the initial seed solution ten times. After 40 and 400 μL of 0.1 м AA solution were added to solution 1 and 2, respectively, both solutions were manually stirred until the complete transparency of solutions. Then, 1200 µL of the diluted seed solution was added to solution 1 (stirred for 1 s), and immediately 3.2 mL of this solution was added to solution 2 (stirred for several seconds). Finally, the obtained solution was kept undisturbed at room temperature for at least 1 h.

Optical Measurements: AuNTs were drop-casted onto the top of monolayer  $WS_2$ . The scattering spectra of single AuNTs on the bare glass substrate or monolayer  $WS_2$  were measured through a dark-field setup consisting of an inverted microscope (Ti-E, Nikon), a spectrograph with an EMCCD camera (Andor), and a halogen white light source (12 V, 100 W).

FDTD Simulations: A commercially available software package (FDTD Solutions, Lumerical) was used to conduct FDTD simulations. The scattered light from the AuNTs was collected in a transmission manner and a plane wave was used as the incident light source. The wavelength-dependent dielectric functions of gold were adapted from Johnson and Christy. The stacked configuration was simulated by placing one AuNT on the top of another one. In SA1, there is a 25 nm overlap between the two AuNTs along the parallel edges. In SA 2, there is a 6 nm overlap between the AuNTs along the perpendicular bisector lines. The edge length of all AuNTs is 55 nm. Because it is highly possible that the suspending tips of upper AuNTs are actually in contact with the substrate, cylinders with the same refractive index (n = 1.44) of the glass substrate were added to those tips to removing additional peaks stemming from the asymmetric dielectric environment.

## **Supporting Information**

Supporting Information is available from the Wiley Online Library or from the author

# **Acknowledgements**

Y.Z., M.W., Z.W., and J.F. acknowledge the financial support of the Office of Naval Research Young Investigator Program (N00014-17-1-2424) and the National Science Foundation (NSF-CBET-1704634 and NSF-CMMI-1761743). A.K. and A.A. acknowledge support from the Welch Foundation with Grant No. F-1802 and the Air Force Office of Scientific Research with MURI Grant No. FA9550-17-1-0002. M.T., T.Z., M.L., and H.L. acknowledge the Air Force Office of Scientific Research (AFOSR) grant No. FA9550-18-1-0072.

### **Conflict of Interest**

The authors declare no conflict of interest.

#### Keywords

2D transition metal dichalcogenides, dark excitons, Fano resonance, gold nanoparticles, plasmonics

Received: February 22, 2019 Revised: May 16, 2019 Published online:

- B. Luk'yanchuk, N. I. Zheludev, S. A. Maier, N. J. Halas, P. Nordlander, H. Giessen, C. T. Chong, Nat. Mater. 2010, 9, 707.
- [2] A. E. Miroshnichenko, S. Flach, Y. S. Kivshar, Rev. Mod. Phys. 2010, 82, 2257.
- [3] J. B. Lassiter, H. Sobhani, J. A. Fan, J. Kundu, F. Capasso, P. Nordlander, N. J. Halas, Nano Lett. 2010, 10, 3184.
- [4] X. Fan, W. Zheng, D. J. Singh, Light: Sci. Appl. 2014, 3, e179.
- [5] C. Yan, K. Y. Yang, O. J. F. Martin, Light: Sci. Appl. 2017, 6, e17017.
- [6] T. Hartsfield, W.-S. Chang, S.-C. Yang, T. Ma, J. Shi, L. Sun, G. Shvets, S. Link, X. Li, Proc. Natl. Acad. Sci. USA 2015, 112, 12288.
- [7] A. Ridolfo, O. Di Stefano, N. Fina, R. Saija, S. Savasta, Phys. Rev. Lett. 2010, 105, 263601.
- [8] R. D. Artuso, G. W. Bryant, Nano Lett. 2008, 8, 2106.
- [9] N. T. Fofang, N. K. Grady, Z. Fan, A. O. Govorov, N. J. Halas, *Nano Lett.* 2011, 11, 1556.
- [10] R. A. Shah, N. F. Scherer, M. Pelton, S. K. Gray, Phys. Rev. B 2013, 88, 075411.
- [11] W. Zhang, A. O. Govorov, G. W. Bryant, Phys. Rev. Lett. 2006, 97, 146804
- [12] S. Manzeli, D. Ovchinnikov, D. Pasquier, O. V. Yazyev, A. Kis, Nat. Rev. Mater. 2017, 2, 17033.
- [13] Q. H. Wang, K. Kalantar-Zadeh, A. Kis, J. N. Coleman, M. S. Strano, Nat. Nanotechnol. 2012, 7, 699.
- [14] D. Jariwala, V. K. Sangwan, L. J. Lauhon, T. J. Marks, M. C. Hersam, ACS Nano 2014, 8, 1102.
- [15] G. M. Akselrod, T. Ming, C. Argyropoulos, T. B. Hoang, Y. Lin, X. Ling, D. R. Smith, J. Kong, M. H. Mikkelsen, *Nano Lett.* 2015, 15, 3578.
- [16] J. Sun, H. Hu, D. Zheng, D. Zhang, Q. Deng, S. Zhang, H. Xu, ACS Nano 2018, 12, 10393.
- [17] M. Wang, W. Li, L. Scarabelli, B. B. Rajeeva, M. Terrones, L. M. Liz-Marzan, D. Akinwande, Y. Zheng, Nanoscale 2017, 9, 13947.
- [18] Y. Kang, S. Najmaei, Z. Liu, Y. Bao, Y. Wang, X. Zhu, N. J. Halas, P. Nordlander, P. M. Ajayan, J. Lou, Z. Fang, Adv. Mater. 2014, 26, 6467.
- [19] Y. Kang, Y. Gong, Z. Hu, Z. Li, Z. Qiu, X. Zhu, P. M. Ajayan, Z. Fang, Nanoscale 2015, 7, 4482.
- [20] M. Wang, A. Krasnok, T. Zhang, L. Scarabelli, H. Liu, Z. Wu, L. M. Liz-Marzán, M. Terrones, A. Alù, Y. Zheng, Adv. Mater. 2018, 30, 1705779.
- [21] M. Stuhrenberg, B. Munkhbat, D. G. Baranov, J. Cuadra, A. B. Yankovich, T. J. Antosiewicz, E. Olsson, T. Shegai, *Nano Lett.* 2018, 18, 5938.
- [22] J. Cuadra, D. G. Baranov, M. Wersall, R. Verre, T. J. Antosiewicz, T. Shegai, Nano Lett. 2018, 18, 1777.
- [23] D. Zheng, S. Zhang, Q. Deng, M. Kang, P. Nordlander, H. Xu, Nano Lett. 2017, 17, 3809.
- [24] W. Liu, B. Lee, C. H. Naylor, H.-S. Ee, J. Park, A. T. C. Johnson, R. Agarwal, Nano Lett. 2016, 16, 1262.
- [25] B. Lee, J. Park, G. H. Han, H.-S. Ee, C. H. Naylor, W. Liu, A. T. C. Johnson, R. Agarwal, *Nano Lett.* 2015, 15, 3646.
- [26] B. Lee, W. Liu, C. H. Naylor, J. Park, S. C. Malek, J. S. Berger, A. T. C. Johnson, R. Agarwal, *Nano Lett.* 2017, 17, 4541.
- [27] J. P. Echeverry, B. Urbaszek, T. Amand, X. Marie, I. C. Gerber, *Phys. Rev. B* 2016, 93, 121107.
- [28] X.-X. Zhang, Y. You, S. Y. F. Zhao, T. F. Heinz, Phys. Rev. Lett. 2015, 115, 257403.
- [29] D. Y. Qiu, F. H. da Jornada, S. G. Louie, Phys. Rev. Lett. 2013, 111, 216805.
- [30] Z. Ye, T. Cao, K. O'Brien, H. Zhu, X. Yin, Y. Wang, S. G. Louie, X. Zhang, *Nature* 2014, 513, 214.
- [31] M. Feierabend, G. Berghauser, A. Knorr, E. Malic, *Nat. Commun.* 2017, 8, 14776.
- [32] M. Selig, G. Berghäuser, A. Raja, P. Nagler, C. Schüller, T. F. Heinz, T. Korn, A. Chernikov, E. Malic, A. Knorr, Nat. Commun. 2016, 7, 13279





- [33] E. Malic, M. Selig, M. Feierabend, S. Brem, D. Christiansen, F. Wendler, A. Knorr, G. Berghäuser, Phys. Rev. Mater. 2018, 2, 014002.
- [34] L. Scarabelli, M. Coronado-Puchau, J. J. Giner-Casares, J. Langer, L. M. Liz-Marzán, ACS Nano 2014, 8, 5833.
- [35] Y. Zhang, Y. Zhang, Q. Ji, J. Ju, H. Yuan, J. Shi, T. Gao, D. Ma, M. Liu, Y. Chen, X. Song, H. Y. Hwang, Y. Cui, Z. Liu, ACS Nano 2013, 7, 8963.
- [36] N. Peimyoo, J. Shang, C. Cong, X. Shen, X. Wu, E. K. L. Yeow, T. Yu, ACS Nano 2013, 7, 10985.
- [37] H. Terrones, E. D. Corro, S. Feng, J. M. Poumirol, D. Rhodes, D. Smirnov, N. R. Pradhan, Z. Lin, M. A. T. Nguyen, A. L. Elías, T. E. Mallouk, L. Balicas, M. A. Pimenta, M. Terrones, Sci. Rep. 2015, 4, 4215.
- [38] A. Berkdemir, H. R. Gutiérrez, A. R. Botello-Méndez, N. Perea-López, A. L. Elías, C.-I. Chia, B. Wang, V. H. Crespi, F. López-Urías, J.-C. Charlier, H. Terrones, M. Terrones, Sci. Rep. 2013, 3, 1755.
- [39] B. Gallinet, O. J. F. Martin, ACS Nano 2011, 5, 8999.
- [40] M. F. Limonov, M. V. Rybin, A. N. Poddubny, Y. S. Kivshar, Nat. Photonics 2017, 11, 543.
- [41] B. Zhu, X. Chen, X. Cui, Sci. Rep. 2015, 5, 9218.

- [42] X. Hong, J. Kim, S.-F. Shi, Y. Zhang, C. Jin, Y. Sun, S. Tongay, J. Wu, Y. Zhang, F. Wang, Nat. Nanotechnol. 2014, 9, 682.
- [43] N. Liu, M. L. Tang, M. Hentschel, H. Giessen, A. P. Alivisatos, *Nat. Mater.* 2011, 10, 631.
- [44] Y. Zhou, G. Scuri, D. S. Wild, A. A. High, A. Dibos, L. A. Jauregui, C. Shu, K. De Greve, K. Pistunova, A. Y. Joe, T. Taniguchi, K. Watanabe, P. Kim, M. D. Lukin, H. Park, Nat. Nanotechnol. 2017, 12, 856.
- [45] X. X. Zhang, T. Cao, Z. Lu, Y. C. Lin, F. Zhang, Y. Wang, Z. Li, J. C. Hone, J. A. Robinson, D. Smirnov, S. G. Louie, T. F. Heinz, Nat. Nanotechnol. 2017, 12, 883.
- [46] M. R. Molas, C. Faugeras, A. O. Slobodeniuk, K. Nogajewski, M. Bartos, D. M. Basko, M. Potemski, 2D Mater. 2017, 4, 021003.
- [47] K.-D. Park, T. Jiang, G. Clark, X. Xu, M. B. Raschke, Nat. Nanotechnol. 2018, 13, 59.
- [48] P. Anger, P. Bharadwaj, L. Novotny, Phys. Rev. Lett. 2006, 96, 113002.
- [49] S. Li, S. Wang, D.-M. Tang, W. Zhao, H. Xu, L. Chu, Y. Bando, D. Golberg, G. Eda, Appl. Mater. Today 2015, 1, 60.
- [50] P. B. Johnson, R. W. Christy, Phys. Rev. B 1972, 6, 4370.